Study of Quasielectic Barrier Distributions as a Step towards the Synthesis of Superheavy Elements with Hot Fusion Reactions

T. Tanaka,[1,2,3] K. Morita,[1,2] K. Morimoto,[1] D. Kaji,[1] H. Haba,[1] R. A. Boll,[4] N. T. Brewer,[4] S. Van Cleve,[4] D. J. Dean,[4] S. Ishizawa,[1,5] Y. Ito,[1,6] Y. Komori,[1] K. Nishio,[6] T. Niwase,[1,2] B. C. Rasco,[4] J. B. Roberto,[4] K. P. Rykaczewski,[4] H. Sakai,[1] D. W. Stracener,[4] and K. Hagino[7,8,9]

[1]*RIKEN Nishina Center for Accelerator-Based Science, Saitama 351-0198, Japan* [2]*Department of Physics, Kyushu University, Fukuoka 819-0395, Japan*

[3]*Department of Nuclear Physics, Research School of Physics and Engineering, The Australian National University, Canberra ACT 2601, Australia*

[4]*Oak Ridge National Laboratory, Tennessee 37831,United States*

[5]*Graduate School of Science and Engineering, Yamagata University, Yamagata 990-8560, Japan*

[6]*Advanced Science Research Center, Japan Atomic Energy Agency, Tokai, Ibaraki 319-1195, Japan*

[7]*Department of Physics, Tohoku University, Sendai 980-8578, Japan*

[8]*Research Center for Electron Photon Science, Tohoku University, Sendai 982-0826, Japan*

[9]*Department of Physics, Kyoto University, Kyoto 606-8502, Japan*

Abstract

The excitation functions for quasielastic scattering of ^{22}Ne+^{248}Cm, ^{26}Mg+^{248}Cm, and ^{48}Ca+^{238}U were measured using the gas-filled-type recoil ion separator GARIS. The quasielastic barrier distributions were extracted for these systems and were compared with coupled-channels calculations. The results indicate that the barrier distribution is affected dominantly by deformation of the actinide target nuclei, but also by vibrational/rotational excitations of the projectile nuclei as well as neutron transfer processes before capture. From a comparison between the experimental barrier distributions and the evaporation residue cross sections for the Sg (Z = 106), Hs (108), Cn (112) and Lv (116) elements, it is suggested that the hot fusion reactions take an advantage of a compact collision geometry with the projectile impacting on the side direction of the deformed target nuclei. A new method is proposed to estimate the optimum incident energy to synthesize unknown superheavy nuclei using the barrier distribution.

PACS numbers:

Atomic nuclei are particularly stabilized when both neutrons and protons have magic numbers. Such nuclei are called doubly magic nuclei: ^{4}He, ^{16}O, ^{40}Ca, ^{48}Ca, and ^{208}Pb are the stable doubly magic isotopes. What will be the next doubly magic nucleus beyond ^{208}Pb? Theoretical physicists have made several different predictions for the next proton magic number, such as Z = 114, 120 and 126 [1–5]. Nuclei located around the next magic number are expected to have a very long half-life than the known superheavy nuclei (SHN), forming "the island of stability". The long-lived SHN would also open a new type of chemistry study for the superheavy elements (SHE), which would necessitate a longer time to complete chemical procedures. The frontier of SHE, between Fl (Z = 114) and Og (Z = 118), has been synthesized by hot fusion reactions using a combination of the ^{48}Ca projectile with actinoid targets [6–10]. A possible signature of the evidence for the island of stability has been found in systematic studies in the SHN region [10], even though the centre of the island has not yet been reached.

A few research groups have attempted (or will attempt) to synthesize new elements, Z = 119 and 120, opening the door to the new period (that is, the 8th period) in the Periodic table, in order to understand the stability of the new SHN [11–15]. In these experiments, heavier projectile nuclei than ^{48}Ca, such as ^{50}Ti, ^{51}V, and ^{54}Cr, are used, since Cf (Z = 98) is the heaviest element which is available with sufficient amounts to make a target material for evaporation residue (ER) measurements [14, 16]. Cross sections of the reactions to produce these new elements are predicted to be much smaller than those for the existing elements [16–19]. They are also known to be sensitive particularly to the incident energy. A new systematic study of the reaction dynamics with the heavier projectile [16, 20–22] is urged since the systematics with the ^{48}Ca projectile would not be sufficient enough to estimate the optimum way to synthesize the new elements, Z = 119 and 120 [16]. Reaction dynamics for the systems in which the ER cross sections are available should be systematically studied in order to extrapolate the optimal beam energy to produce these new SHE.

One of the most direct ways to understand the reaction mechanism and determine the optimum incident energy, at which the evaporation residue cross section is maximized, will be provided by the capture barrier distribution[23–25]. In heavy-ion reactions, the Coulomb barrier is strongly modified by couplings of the relative motion between the colliding nuclei to several nuclear excitations [26] as well as nucleon transfer processes [27]. Such couplings lead to a distribution of the Coulomb barriers [26, 28]. The barrier distribution can be obtained either from fusion reactions[28] or from quasielastic (QE) scattering [29], which is defined as the sum of all reaction processes other than fusion (i.e., elastic scattering, inelastic scattering, and direct transfer channels). Many experimental studies have established the validity of the concept of the barrier distribution [26, 30], and coupled-channel calculations have been successfully compared to the experimentally determined barrier distributions [30, 34].

The barrier distribution refers to a barrier for a two-body system to reach the touching configuration. In medium-heavy systems, the compound nucleus is automatically formed once the touching configuration is reached. Therefore, the barrier distribution has customarily been referred to as the "fusion" barrier distribution. In contrast, in the superheavy region, due to the quasifission process, the compound nucleus is not necessarily formed even if the touching configuration is reached [32, 33]. In that situation, it would be more appropriate to call it the "capture" barrier distribution.

In Ref. [25], the first result of a QE barrier distribution measurement using the gas-filled recoil ion separator GARIS[35, 36] was reported. In the measurement, the quasi-elastic cross sections for the angular momentum $l \sim 0$ were successfully obtained by measuring the target nuclei recoiling into the forward angle (which corresponds to $\theta_{\rm lab} \sim 180°$) [25]. This was in a marked contrast to the previous QE barrier distribution studies [23, 24, 29], which measured the recoiled projectile-like nuclei at backward angles ($\theta_{\rm lab} \sim 170°$ or smaller). An advantage to take experimental data at $l \sim 0$ is that one does not necessary to map the data onto those at $l \sim 0$ using the effective energy [37], and thus a direct comparison between a measured barrier distribution and experimental evaporation residue (ER) cross-sections, $\sigma_{\rm ER}$, is possible.

In this Letter, we apply the same method as in Ref. [25] to the ^{22}Ne+^{248}Cm, ^{26}Mg+^{248}Cm, and ^{48}Ca+^{238}U reactions, relevant to hot fusion reactions for the production of SHN Sg ($Z = 106$), Hs ($Z = 108$), and Cn ($Z = 112$), respectively, in order to carry out a systematic study on the reaction dynamics for new SHEs. For this purpose, we combine the results to that of our previous measurement for the ^{48}Ca+^{248}Cm reaction, relevant to a synthesis of Lv ($Z = 116$) [25].

Whereas the previous measurement discussed the difference in the optimum incident energy for cold (^{48}Ca+^{208}Pb and ^{50}Ti+^{208}Pb) and hot (^{48}Ca+^{248}Cm) fusion reactions [25], in this paper we use the systematic data to discuss mainly the fusion dynamics for hot fusion reactions towards a synthesis of the new SHN and SHE.

The experiments were performed at the RIKEN RILAC facility. Beams were prepared from an 18 GHz ECR ion source[38] feeding the RIKEN heavy-ion linear accelerator (RILAC)[39] for ^{22}Ne^{6+}, ^{26}Mg^{7+} ions, and using the micro-oven technique[40] for ^{48}Ca^{11+} ion. The beam energy was measured by two methods: with the magnetic rigidity of the ions traversing a 90° bending magnet and by time-of-flight measurements. The accuracy of these systems is 0.2%. The beam intensity was following: 15 - 300 pnA for ^{22}Ne, 1.3 - 130 pnA for ^{26}Mg, and 9.2 - 920 pnA for ^{48}Ca (1 pnA correspond to 6.2×10^9 particle per second). The beam intensities were adjusted to optimum intensities based on the statistics of the events and dead time of the focal plane detectors.

The ^{248}Cm$_2$O$_3$ targets were produced by electrodeposition of the material on 2.2-μm-thick Ti backing foil[41]. The thickness of the ^{248}Cm$_2$O$_3$ layer deposit were 490 μg/cm^2. The 10-cm-radius target wheel contained eight arc-shaped targets, and it was rotated at 1000 rpm during the beam irradiation. Same as the ^{248}Cm$_2$O$_3$ targets, the ^{238}U$_3$O$_8$ targets were produced by electrodeposition of the material on 3.0-μm-thick Ti backing foil, and the thickness was 310 μg/cm^2. The 30-cm-radius target wheel for ^{238}U$_3$O$_8$ targets contained sixteen arc-shaped targets, and it was rotated at 2000 rpm during the beam irradiation. The recoiled target-like events were separated from the background events by the gas-filled-type recoil ion separator GARIS[35, 36].

The separator was filled with pure helium gas of 100 Pa for ^{22}Ne+^{248}Cm,111 Pa for ^{26}Mg+^{248}Cm, 133 Pa for ^{48}Ca+^{238}U. Magnetic rigidity parameter of GARIS was changed and optimized for every energy point with events measured by the 16-strip position-sensitive silicon detector (PSD). The magnetic rigidity of GARIS was typically set 1.97 Tm for ^{22}Ne+^{248}Cm, 1.96 Tm for ^{26}Mg+^{248}Cm, 1.68 Tm for ^{48}Ca+^{238}U.

The focal plane detectors were consisted of ToF detectors and a 16-strip PSD. The ToF detectors use electron-emission foil made of a 0.5-μm Mylar foil coated with 0.01-μm Au and 20-μg/cm^2 CsI. The efficiency of the ToF detectors were almost 100% for target-like events. The PSD detector has an active area of 58×58 mm^2 and is divided to 16 strips. A precise energy calibration of the PSD strips was performed on the basis of decay line from ^{241}Am source. The events of our experiment were sorted energy by energy. The data acquisition system was started by the signal measured by the PSD. The electronic discriminator level was set to approximately 1 MeV.

Rutherford scattering events were measured using a Silicon detector for the normalization of measured the excitation functions using the Rutherford scattering cross section. The detector had an active area of 3.6×3.6 mm^2, and was mounted either 25 cm or 142 cm downstream of the target at 45° with respect to the beam axis, since in our calculation, 45° elastic scattering events at all energy points follow Rutherford scattering.

Figures 1 (a) and (b) show a typical two-dimensional (2D) plot of the content of the time of flight versus energy (ToF-E) matrix for the reactions ^{48}Ca+^{238}U at $E_{\mathrm{c.m.}}$ = 165.1 MeV and $E_{\mathrm{c.m.}}$ = 203.7 MeV, respectively. From the point of view of the kinematics calculations and considering that tantalum is present in the beam path, the events in the 2D plots were classified as ^{238}U target-like events, ^{181}Ta sputtered by impinging beam from beam stopper, ^{181}Ta sputtered by impinging beam from beam slits, ^{48}Ca beam-like events.

Figure 1 (c) show the strip distribution of the PSD for reactions ^{48}Ca+^{238}U at $E_{\mathrm{c.m.}}$ = 165.1 MeV. The PSD was consisted of the strip-0 to strip-15 silicon detectors. The strip-0 was located on the higher magnetic rigidity side, and the strip-15 was on the opposite side. The strip distribution of the strip-1 to strip-15 was used for the present analyses since the strip-0 was out of order. The extension of this distribution slightly exceeds the PSD size. A Gaussian distribution (the green line) well reproduced the obtained experimental strip distribution, which enabled us to estimate the total counts of target-like events. The integral value of the Gaussian distribution was defined as the exact count for QE scattering events.

The transmission efficiencies of GARIS [42] changes with respect to v/v_0 of the nuclei that fly in GARIS (v and v_0 refer to the velocity of the nuclei and Bohr velocity, respectively). The v/v_0 values in this work were 2.08 - 2.49 for ^{22}Ne+^{248}Cm, 2.41 - 2.95 for ^{26}Mg+^{248}Cm, and 4.27 - 4.99 for ^{48}Ca+^{238}U. According to Ref. [42], the strip distribution is widen due to the multiple scattering, and the transmission efficiency is decreased. Since the yield of QE events were revised by the Gaussian function fitting from the strip distribution, the reductions from the transmission efficiency were also revised from the previous procedures.

The experimental results, indicated by the red or green symbols, are shown in Figs. 2 and 3. The error bars account the statistical as well as systematic uncertainties [43]. The green symbols indicate the experimental data points in which QE and deep-inelastic (DI) scattering events are mixed together. These data points provide an upper limit for $d\sigma_{\mathrm{QE}}/d\sigma_{\mathrm{R}}$. See Ref. [43] for further details of the experiment.

The experimental results were interpreted by the coupled-channels approach on the basis of the

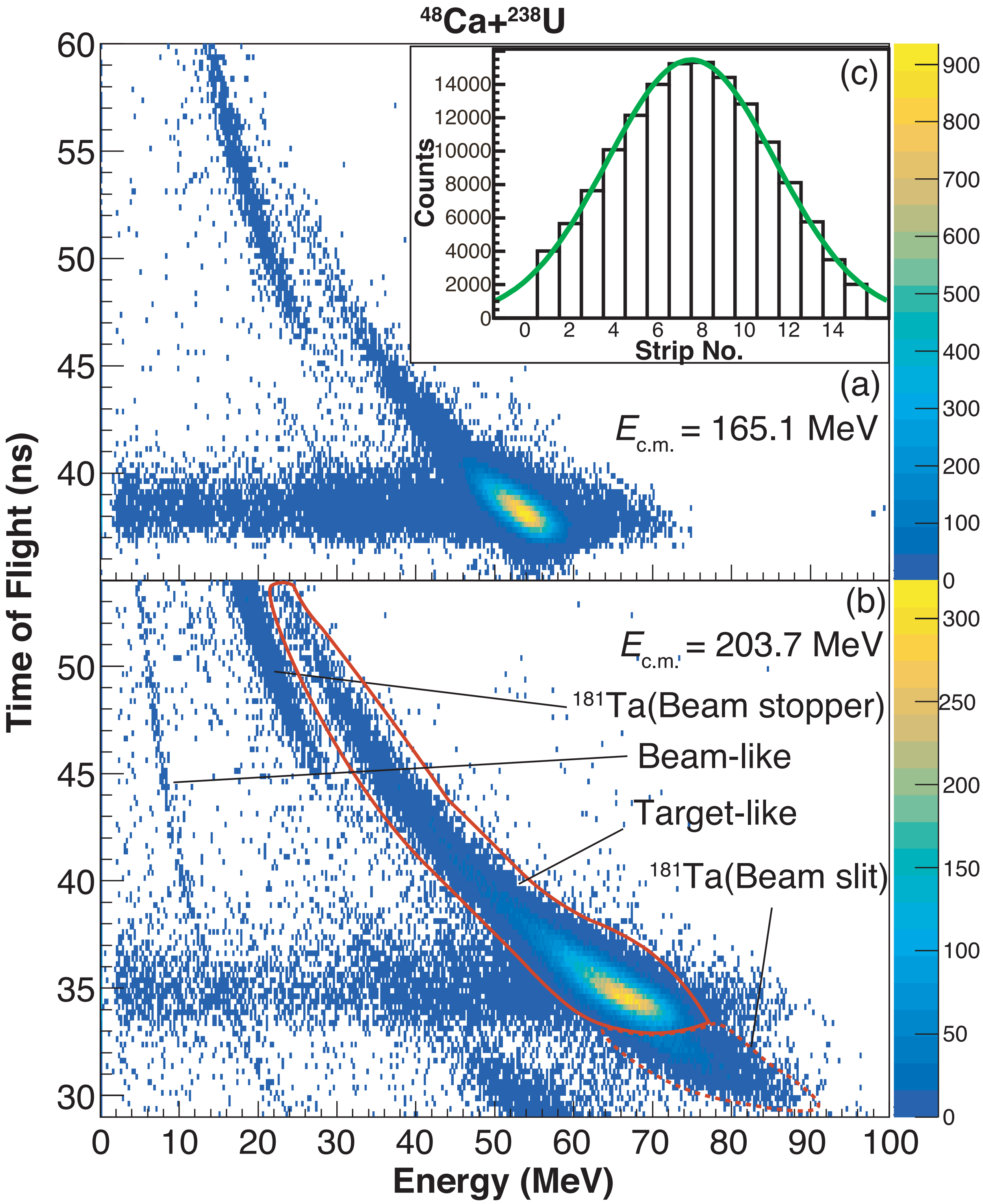

FIG. 1: Two-dimensional plots of the time of flight (ToF) versus the energy, E. The vertical axis shows the time of flight measured by ToF detectors, and the horizontal axis shows the energy detected by the PSD at (a) $E_{\mathrm{c.m.}}$ = 165.1MeV and (b) $E_{\mathrm{c.m.}}$ = 203.7MeV. The panel (c) shows the strip distribution of target-like events (the black line boxes) with the Gaussian fit of the distribution (the green line). The integral value of the Gaussian fit was used as an estimate of the exact value of QE scattering events.

computer code CCFULL [31, 44], in which a Woods-Saxon potential is employed for an internuclear potential. The parameters of the real part of the potential which were used in the present analyses were $r_0 = 1.18$ fm and $a_0 = 0.69$ fm, for the radius and the diffuseness parameters, respectively. Those of the imaginary part were $r_\mathrm{w} = 1.0$ fm, $a_\mathrm{w} = 0.4$ fm, and $V_\mathrm{w} = 50$ MeV. The radius and diffuseness parameters of the real part of the potential for each system were close to those of the Akyüz-Winther potential [45]. Following the previous works [24, 25], the depth parameter V_0 of the real part of the internuclear potential was adjusted to reproduce the measured excitation functions.

The dashed blue curves in Fig. 2 show the results with the deformation effect of the target

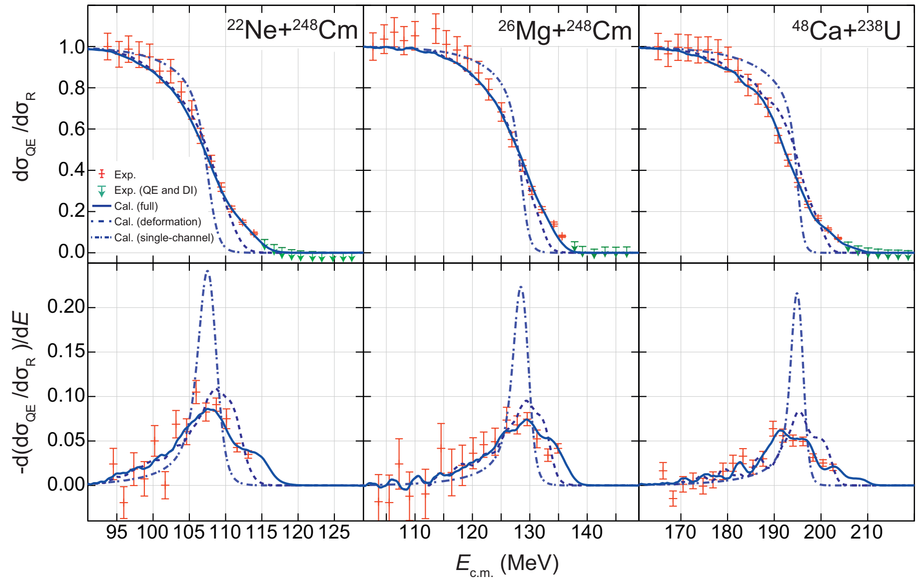

FIG. 2: The measured excitation functions for the QE scattering cross section relative to the Rutherford cross section (the top panels), and the corresponding QE barrier distribution (the lower panels). The left, the middle, and the right panels are for the ^{22}Ne+^{248}Cm, ^{26}Mg+^{248}Cm, and ^{48}Ca+^{238}U systems, respectively. The red symbols indicate the experimental data from this work, for which the error bars include the statistical and systematic uncertainties. The green symbols indicate the experimental data in which QE and the deep-inelastic (DI) events are mixed together. These data points provide upper limits for $d\sigma_{QE}/d\sigma_R$. The blue solid curves denote the best fit of the coupled-channels calculation. The blue dash-doted curves show the results of the single-channel calculations, while the blue dotted curves show the results which took into account only the deformation effect of the target nuclei, both with the same internuclear potential as that used for the blue solid lines.

nuclei. To this end, the deformation parameters of $\beta_2 = 0.2972$ [46], $\beta_4 = 0.039$ [47], and $\beta_6 = 0.030$ for ^{248}Cm, and $\beta_2 = 0.2860$ [46], $\beta_4 = 0.050$ [34], and $\beta_6 = 0.050$ for ^{238}U were employed. For a comparison, the figure also shows the results of the no-coupling case by the dot-dashed lines. From a comparison of these two results, one can clearly see that the barrier distributions are strongly influenced by the deformation effect of the target nuclei.

We then included the couplings to low-lying collective excitations in the projectile nuclei as well as a neutron transfer process before the capture using the orientation average formula [37] for the deformed targets. For the collective excitations, we considered the quadrupole phonon excitations in ^{22}Ne and ^{26}Mg at 1.27 MeV with $\beta_2 = 0.562$ and at 1.808 MeV and $\beta_2 = 0.487$, respectively [46], as well as the octupole phonon excitation in ^{48}Ca at 4.507 MeV with $\beta_3 = 0.1748$ [48]. The transfer Q-values were taken to be those for the ground state to the ground state transitions, Q_{gg}, which were estimated based on mass table in Ref.[47]. The coupling strengths to the transfer channels were adjusted for each system to reproduce the data, as in Ref. [25]. The calculated results are shown in Fig. 2 and Fig. 3 by the solid blue lines. The experimental data are well reproduced by these calculations, indicating that the barrier distributions are significantly altered by the excitions of the projectile nuclei and the neutron transfer, even though the deformation of the target nuclei provides a major contribution.

The experimental excitation functions for the evaporation residue (ER) cross sections [8, 49–56] were shown in the bottom panels of Fig. 3. The solid and the dashed arrows indicate the experimentally determined average Coulomb barrier height, B_0, at which $\mathrm{d}\sigma_{\mathrm{QE}}/\mathrm{d}\sigma_{\mathrm{R}}$ is 0.5, and the Coulomb barrier height of the side collision, B_{side}, respectively. Here, B_{side} was determined as follows. In the coupled-channels calculations, CCFULL employs a deformed Woods-Saxon potential, which leads to orientation angle dependent barrier heights, $B(\theta)$ [31]. One can then define the (theoretical) average barrier height as

$$\bar{B} = \frac{\int_0^{\frac{\pi}{2}} B(\theta)\sin(\theta)d\theta}{\int_0^{\frac{\pi}{2}} \sin(\theta)d\theta}. \tag{1}$$

The same values for the parameters of r_0, a_0,r_w, a_w, V_w, β_2, β_4 and β_6, as those in the CCFULL calclulations were used to calculate the B_{side}. The s-wave scattering was assumed, since our experimental method yields the experimental Coulomb barrier distribution for $l \sim 0$. The depth of the Woods-Saxon potential is adjusted so that the average barrier height, $\bar{B}$, coincides with the experimental average barrier height, B_0, which eventually defines B_{side} as $B_{\mathrm{side}} = B(90^\circ)$. Note that the above (below) barrier region corresponds to the side (tip) collision, which corresponds to the

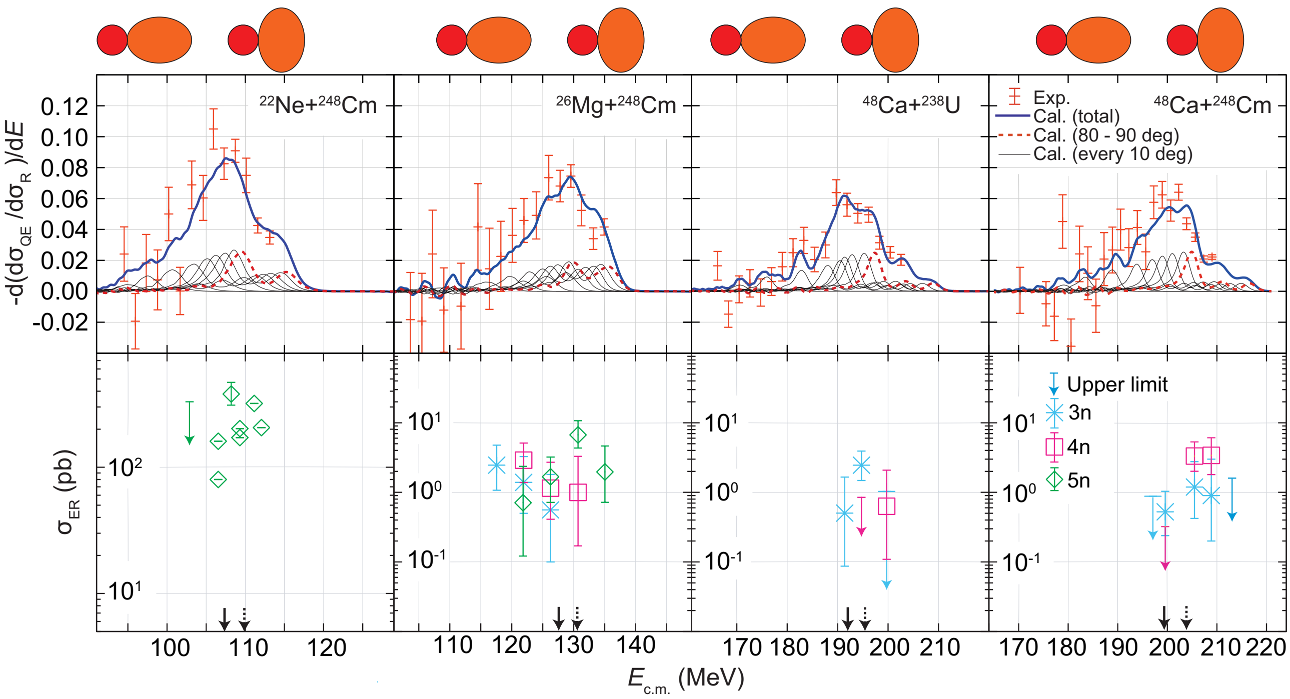

FIG. 3: A comparison between the measured QE barrier distributions (the upper panels) and the evaporation residue cross sections reported at different center-of-mass energies for the syntheses of Sg (Z = 106), Hs (Z = 108), Cn (Z = 112), and Lv(Z = 116) [8, 49–56] (the lower panels). The panels are for the ^{22}Ne+^{248}Cm, ^{26}Mg+^{248}Cm, ^{48}Ca+^{238}U, and ^{48}Ca+^{248}Cm systems from left to right. The meaning of the red symbols and the blue solid curves are the same as in Fig. 2. The red dotted lines show the barrier distribution for the 80 - 90° for the orientation angle of the target nuclei with respect to the beam direction. The black thin lines show the barrier distribution for every 10°, such as 0° - 10°, 10° - 20°,..., 70° - 80°. The solid and the dashed black arrows denote the average Coulomb barrier height B_0, corresponding to the energy point at which $d\sigma_{QE}/d\sigma_R$ is 0.5, and the Coulomb barrier height of the side collision B_{side}, respectively.

higher (lower) energy side in the top panels in Fig. 3 when the deformation of the target is taken into account.

By comparing among (i) the peak of the ER cross sections, (ii) B_0 and (iii) B_{side}, it is realized that the peaks of the ER cross sections appear above the B_0 and close to B_{side}, even though B_{side} may contain theoretical systematic errors due to uncertainties in the deformation parameters (e.g., B_{side} is altered from 109.9 MeV to 111.9 MeV when β_4 and β_6 are switched off for the ^{22}Ne+^{248}Cm reaction). Even if we have taken into account such uncertainties, the results clearly indicate that the evaporation residue cross sections are maximized for a compact collision. That is, in the compound nucleus (CN) formation process, the probability of CN formation increases for the side collision because of the shorter distance of the centre of nuclei at the touching configuration, as has been discussed in Refs. [25, 34, 57].

The red dotted lines in Fig 3 shows the barrier distribution for the 80 – 90°, while the black thin solid lines are for the barrier distribution for every 10°, that is, 0° - 10°, 10° - 20°,..., 70° - 80°. The total barrier distributions, which are the sum of the black thin solid lines and the red dotted lines, are also shown by the blue solid lines. Notice that the Coulomb barrier distribution for 80 – 90° coincides with $B_{\rm side}$, which is widened due to the other couplings such as the inelastic excitations of the projectile nuclei and the neutron transfer channel. Of course, the peak of the ER cross sections coincide not only with the barrier distribution for 80 – 90°, but also with that for 70 – 80° etc. However, the overlap with the barrier distribution for the tip collision, such as 0° - 20°, is negligibly small, indicating that these hot fusion reactions take an advantage of the compact collision.

A comparison between the total barrier distribution and the individual barrier distributions implies that the effect of the target deformation is stronger in widening the barrier distribution as compared to that of the other couplings, even though the latter also contributes significantly. Evidently, several coupling effects, including the deformation and the inelastic excitations in the colliding nuclei, should be taken into account in theoretical calculations to understand the reaction mechanism for synthesizing superheavy nuclei with hot fusion reactions.

We point out that the optimum incident energy for hot fusion reaction can be estimated by an experimentally determined barrier distribution as indicated in this Letter, if the trend of compact collision is not changed. Importantly, it would take only about one day to measure a barrier distribution for one reaction, which is much shorter than a typical experiment to synthesize new SHE, e.g., more than 100 days using one pμA beam (6.2×10^{12} particle per second). This new method will significantly contribute to future experiments to synthesis both new SHE and SHN in the island of stability. Another important fact is that this determination is almost independent of theoretical predictions, which may include a large model dependence.

In conclusion, the excitation functions of quasielastic scattering cross sections for reactions relevant to the syntheses of superheavy nuclei, that is, the ^{22}Ne+^{248}Cm, ^{26}Mg+^{248}Cm, and ^{48}Ca+^{238}U systems, were measured to understand the reaction dynamics of hot fusion reactions. Coupled-channels calculations were performed by taking into the deformation effect of the target nuclei.

The experimental data were well reproduced by the calculations, which demonstrates the importance of the deformation of the target nuclei. From a comparison between the experimentally determined barrier distribution and the ER cross-sections for Sg (Z = 106), Hs (Z = 108), Cn (Z = 112) and Lv (Z = 116), the ER cross-sections peak at an energy in between the average Coulomb barrier height and that for the side collision, where the projectile approaches along the short axis of a prolately deformed nucleus. Moreover, it was also found that the peaks coincide with the Coulomb barrier distribution for compact collisions, such as 70 − 90°. This suggests that the evaporation residue cross sections are enhanced at energies that correspond to a compact collision geometry with the projectile impacting on the side of the deformed target nucleus.

We advocate that a measurement of the barrier distribution provides a powerful tool for understanding the underlying reaction dynamics for synthesizing an unknown very heavy nuclide. In particular, it is woth noting that it provides an efficient way to determine the optimal bombarding energy for synthesis new superheavy elements.

The experiments of this study were performed at the RI Beam Factory operated by RIKEN Nishina Center and CNS, University of Tokyo. We would like to thank the accelerator staffs for their excellent operation and assistance during the experiments. In particular, we are grateful to Dr. M. Kidera for providing stable beams and RILAC accelerator operators for managing several fast energy changes during the night and day. ^{248}Cm material was provided by the U.S. DOE Isotope Program. This research was partially supported by a Grant-in-Aid for Specially Promoted Research, 19002005, 2007, from the Ministry of Education, Culture, Sports, Science and Technology of Japan. T.T. thanks the RIKEN Junior Research Associate Program.

---

[1] A. Sobiczewski, F. A. Gareev, and B. N. Kalinkin, Phys. Lett. **22**, 500 (1966).

[2] W. D. Myers and W. J. Swiatecki, Nucl. Phys. **81**, 1 (1966).

[3] U. Mosel and W. Greiner, Z. Phys. **222**, 261 (1969).

[4] M. Bender, K. Rutz, P. G. Reinhard, J. A. Maruhn, and W. Greiner, Phys. Rev. C **60**, 034304 (1999).

[5] H. Koura, Prog. Theor. Exp. Phys. 113D02, (2014).

[6] Yu. Ts. Oganessian *et al.*, Phys. Rev. C **69**, 021601(R) (2004).

[7] Yu. Ts. Oganessian *et al.*, Phys. Rev. C **69**, 054607 (2004).

[8] Yu. Ts. Oganessian *et al.*, Phys. Rev. C **70**, 064609 (2004).

[9] Yu. Ts. Oganessian *et al.*, Phys. Rev. C **74**, 044602 (2006).

[10] Yu. Ts. Oganessian *et al.*, Phys. Rev. Lett. **104**, 142502 (2010).

[11] C. E. Düllmann, EPJ Web Conf. **131**, 08004 (2016).

[12] S. Hofmann *et al.*, Eur. Phys. J. A **52**, 180 (2016).

[13] S. Dmitrieva *et al.*, EPJ Web of Conf. **131**, 08001 (2016).

[14] C. E. Düllmann, EPJ Web of Conf. **163**, 00015 (2017).

[15] T. Tanaka and K. Morita, AAPPS Bulletin Vol. **28** No. 3, 28 (2018).

[16] V. I. Zagrebaev and W. Greiner, Phys. Rev. C **78**, 034610 (2008).

[17] L. Zhu, W. J. Xie, and F. S. Zhang, Phys. Rev. C **89**, 024615 (2014).

[18] N. Ghahramanya and A. Ansari, Eur. Phys. J. A **52**, 287 (2016).

[19] G. G. Adamian, N. V. Antonenko, and H. Lenske, Nucl. Phys. A **970**, 22 (2018).

[20] K. Hagino, Phys. Rev. C **98**, 014607 (2018).

[21] Y. Aritomo *et al.*, JPS Conf. Proc. **23**, 013001 (2018).

[22] K. Sekizawa and K. Hagino, Phys. Rev. C **99**, 051602(R).

[23] S. S. Ntshangase *et al.*, Phys. Lett. B **651**, 27 (2007).

[24] S. Mitsuoka *et al.*, Phys. Rev. Lett. **99**, 182701 (2007).

[25] T. Tanaka *et al.*, J. Phys. Soc. Jpn. **87**, 014201 (2018).

[26] M. Dasgupta *et al.*, Ann. Rev. Nucl. Sci. **48**, 401(1998).

[27] A. B. Balantekin and N. Takigawa, Rev. Mod. Phys. **70**, 77 (1998).

[28] N. Rowley, G.R. Satchler, and P.H. Stelson, Phys. Lett. B **254**, 25 (1991).

[29] H. Timmers *et al.*, Nucl. Phys. A **584**, 190 (1995).

[30] J. R. Leigh *et al.*, Phys. Rev. C **52**, 3151 (1995).

[31] K. Hagino and N. Takigawa, Prog. Theor. Phys. **128**, 1061(2012).

[32] G.G.Adamian, N.V.Antonenko, and W.Scheid, Nucl. Phys. A **678**, 24 (2000).

[33] D. J. Hinde, M. Dasgupta, and A. Mukherjee, Phys. Rev. Lett. **89**, 282701 (2002).

[34] D. J. Hinde *et al.*, Phys. Rev. Lett. **74**, 1295 (1995).

[35] K. Morita *et al.*, Nucl. Instrum. Methods B **70**, 220 (1992).

[36] K. Morita *et al.*, Eur. Phys. J. A **21**, 257 (2004).

[37] K. Hagino and N. Rowley, Phys. Rev. C **69**, 054610 (2004).

[38] T. Nakagawa *et al.*, Nucl. Instrum. Methods B **226**, 392 (2004).

[39] M. Odera *et al.*, Nucl. Instrum. Methods. **227**, 187 (1984).

[40] K. Ozeki, T. Kageyama, M. Kidera, Y. Higurashi, and T. Nakagawa, Rev. Sci. Instrum. **86**, 016114 (2015).

[41] Y. Kudou, H. Haba, K. Ooe, D. Kaji, K. Morimoto, A. Shinohara, and K. Morita, RIKEN Accel. Prog. Rep. **42**, 265 (2009).

[42] D. Kaji, K. Morita, K. Morimoto, H. Haba, and H. Kudo, Proc. Radiochim. Acta **1**, 105 (2011).

[43] T. Tanaka, Doctoral dissertation, Kyushu University (2019). `https://catalog.lib.kyushu-u.ac.jp/opac_download_md/2236025/sci1328.pdf`

[44] K. Hagino, N. Rowley, and A. T. Kruppa, Comput. Phys. Commun. **143**, 123 (1999).

[45] O. Akyuz and A. Winther, *in Proceedings of the International School of Physics "Enrico Fermi" Course LXXVII, Varenna, 1979, edited by R. A. Broglia, C. H. Dasso, and R. A. Ricci* (North-Holland, Amsterdam, 1981), p. 492.

[46] S. Raman, C. W. Nestor, Jr., and P. Tikkanen, At. Data Nucl. Data Tables **78**, 1 (2001).

[47] P. Moller *et al.*, At. Data Nucl. Data Tables **109-110**, 1-204 (2016).

[48] R. H. Spear, At. Data Nucl. Data Tables **42**, 55 (1989).

[49] Yu. A. Lazarev *et al.*, Phys. Rev. Lett. **73**, 624 (1994).

[50] A. Türler *et al.*, Phys. Rev. C **57**, 1648 (1998).

[51] R. Dressier, B. Eichler, D. T. Jost, A. Tiirler, R. Eichler, H. W. Gäggeler, PSI Rep. **1**, p.130 (1999).

[52] S. Hübener *et al.*, Radiochimica Acta **89**, 737 (2001).

[53] H. Haba *et al.*, Phys. Rev. C **85**, 024611 (2012).

[54] J. Dvorak *et al.*, Phys. Rev. Lett. **100**, 132503 (2008).

[55] S. Hofmann *et al.*, Eur. Phys. J. A **32**, 251 (2007).

[56] S. Hofmann *et al.*, Eur. Phys. J. A **48**, 62 (2012).

[57] K. Nishio, H. Ikezoe, S. Mitsuoka, and J. Lu, Phys. Rev. C **62**, 014602 (2000).